The Journal of Chemical Physics

RESEARCH ARTICLE | DECEMBER 01 2025

System–bath modeling in vibrational spectroscopy via molecular dynamics: A machine learning framework for hierarchical equations of motion (HEOM)

Special Collection: Festschrift in honor of Minhaeng Cho: Ultrafast Spectroscopy

Kwanghee Park ; Ju-Yeon Jo ; Yoshitaka Tanimura

Check for updates

J. Chem. Phys. 163, 214104 (2025)
https://doi.org/10.1063/5.0300203

View Online
Export Citation

Articles You May Be Interested In

Quantum hierarchical Fokker–Planck equations with U(1) gauge fields: Application to the Aharonov–Bohm ring

J. Chem. Phys. (October 2025)

Numerically "exact" simulations of entropy production in the fully quantum regime: Boltzmann entropy vs von Neumann entropy

J. Chem. Phys. (December 2020)

Reduced quantum dynamics with arbitrary bath spectral densities: Hierarchical equations of motion based on several different bath decomposition schemes

J. Chem. Phys. (April 2014)

01 December 2025 21:12:15

Webinar From Noise to Knowledge
May 13th – Register now
Zurich Instruments
Universität Konstanz

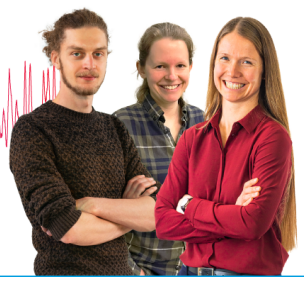

AIP Publishing

The Journal of Chemical Physics ARTICLE pubs.aip.org/aip/jcp

System–bath modeling in vibrational spectroscopy via molecular dynamics: A machine learning framework for hierarchical equations of motion (HEOM)

Cite as: J. Chem. Phys. 163, 214104 (2025); doi: 10.1063/5.0300203
Submitted: 31 August 2025 • Accepted: 30 October 2025 •
Published Online: 1 December 2025

View Online Export Citation CrossMark

Kwanghee Park,[1,a)] Ju-Yeon Jo,[2] and Yoshitaka Tanimura[1,a)]

AFFILIATIONS

[1] Department of Chemistry, Graduate School of Science, Kyoto University, Kyoto 606-8502, Japan
[2] Graduate School of Energy Science, Kyoto University, Kyoto 606-8502, Japan

Note: This paper is part of the Special Topic, Ultrafast Spectroscopy and Dynamics.
[a)] **Authors to whom correspondence should be addressed:** park.kwanghee.v48@kyoto-u.jp and tanimura.yoshitaka.5w@kyoto-u.jp

ABSTRACT

Molecular vibrations in solutions, especially OH stretching and bending in water, drive ultrafast energy relaxation and dephasing in chemical and biological systems. We present a machine learning approach for constructing system–bath models of intramolecular vibrations in solution, compatible with quantum simulations via the hierarchical equations of motion (HEOM). Using classical molecular dynamics trajectories generated with a force field specifically developed for intramolecular modes, the model captures anharmonic mode coupling and non-Markovian dissipation through spectral distribution functions (SDFs). These results enable a fully quantum mechanical description of ultrafast energy relaxation and vibrational dephasing processes in the presence of quantum heat baths within the HEOM framework. The trained model yields physically interpretable parameters, validated against infrared spectra. Notably, we demonstrate that synergistically integrating a Brownian oscillator (BO) SDF and a Drude SDF—representing intermolecular and intramolecular vibrational relaxation, respectively—substantially improves learning efficiency for nuclear trajectories. However, the linear absorption spectrum calculated by this model is accurately reproduced in the Drude-only SDF case, as incorporating intermolecular vibrational effects solely within the BO SDF leads to their overestimation. Possible remedies to this issue are also discussed.

Published under an exclusive license by AIP Publishing. https://doi.org/10.1063/5.0300203

01 December 2025 21:12:15

I. INTRODUCTION

Modern molecular laser spectroscopy involves the sequential irradiation of a sample with ultrafast laser pulses at precisely controlled time intervals. The resulting spectroscopic observables are governed by nonlinear response functions and reflect complex intermolecular and intramolecular dynamics. Interpreting these spectra remains a persistent challenge due to the intricate nature of the underlying molecular interactions.[1–5]

While molecular dynamics (MD) simulations hold promise for capturing intricate spectral signatures—particularly in two-dimensional (2D) spectroscopy—their foundation in classical mechanics inherently constrains the precision of peak positions and line shapes.[6–12] To accurately capture nonlinear phenomena such as the 2D infrared (IR) echo spectrum, it is essential to incorporate the quantum entanglement between molecular motion and its surrounding environment,[13–15] herein referred to as "bathentanglement."[16] Thus, a quantum mechanical framework —such as the hierarchical equations of motion (HEOM)—is indispensable for elucidating the underlying quantum thermodynamics responsible for the observed spectral features.[17–20]

Model-based approaches have emerged as practical, flexible, and effective tools for simulating nonlinear vibrational spectra.[13–15] By introducing a thermal bath that reflects environmental influences on primary vibrational modes, these models enable the computation of various nonlinear spectra. One such strategy describes vibrational

Published under an exclusive license by AIP Publishing

relaxation and dephasing using Brownian, exciton, and stochastic models.[13–15,21–24] These models incorporate energy states and noise spectral distribution functions (SDFs) that are evaluated from MD simulations or spectroscopic experiments.

While conventional approaches often struggle to capture intricate vibrational mode couplings and non-Markovian environmental effects, the multi-mode anharmonic Brownian model provides a versatile framework grounded in the theory of open quantum systems.[15] This model systematically incorporates anharmonic interactions among vibrational modes, along with both homogeneous and inhomogeneous spectral broadening.[25–31] Its dynamics are computed using the hierarchical equations of motion (HEOM), a numerically "exact" formalism that rigorously accounts for the quantum effects of the thermal environment beyond perturbative and Markovian limits.[16,32]

Spectral simulations based on the HEOM formalism have been successfully applied to a range of problems,[16] including 2D vibrational spectroscopies.[32–34] The model description and computational accuracy have been validated, but the overall performance depends critically on the choice of model parameters.

To date, the selection of parameters and SDFs within this framework has relied predominantly on empirical tuning of MD simulations, with the primary objective of reproducing experimentally observed spectral features across a range of modalities—including infrared absorption, off-resonant Raman, two-dimensional (2D) Raman,[34] 2D Terahertz-Raman,[26,31] 2D infrared-Raman,[27,28] and 2D infrared spectroscopy.[29,30]

While this heuristic approach has yielded qualitative agreement in many cases, it remains inherently unsystematic and computationally intensive. Furthermore, its generalizability is constrained by a fundamental limitation: the intensity of spectroscopic observables does not necessarily correlate with the intrinsic strength of individual vibrational modes. This ambiguity becomes especially pronounced in scenarios where distinct vibrational modes exhibit degenerate frequencies or when spectroscopically silent or dark modes are present, thereby obfuscating the interpretation of spectral signatures.

In this study, we employ a machine learning (ML) framework to directly extract model parameters and SDFs of thermal baths from MD trajectories.[35,36] Previous efforts to construct such models resulted in SDFs that were too intricate to be incorporated into the HEOM framework, thereby precluding spectral simulations.[35] Here, we retain the model structure used in earlier studies but refine the parameters by constraining the SDFs to forms compatible with the HEOM formalism. We demonstrate this approach using liquid water, a system for which extensive 2D spectroscopic data are available from both experiments and simulations. Our method complements ongoing developments in classical and quantum HEOM-based computational schemes.[29–31]

This paper is structured as follows: Sec. II introduces the multimode anharmonic Brownian (MAB) model with nonlinear system–bath (S–B) interactions, with particular emphasis on molecular liquids as the target system. The ML algorithm used to extract the model parameters is also described. Section III presents the evaluation and analysis of the model parameters for three intramolecular vibrational modes of liquid water. Finally, Sec. IV provides the concluding remarks.

II. THEORY

A. Multimode anharmonic Brownian (MAB) model

To simulate both linear and nonlinear vibrational spectra of molecules in condensed phases, we adopt the MAB model. In this framework, anharmonic intramolecular vibrational modes are nonlinearly coupled to surrounding molecular modes, which are treated as multiple bath systems. Each bath is represented by an ensemble of harmonic oscillators. This model provides a versatile and systematic approach to incorporating anharmonic mode–mode coupling in the context of open quantum dynamics theory.

Homogeneous and inhomogeneous broadening effects are accounted for via nonlinear and non-Markovian S–B interactions.[37–40] The HEOM formalism enables the direct computation of 2D vibrational spectra for a range of molecular liquids, including water.[28–34]

The total Hamiltonian of the MAB model is formulated as follows:[25–31]

$$\hat{H}_{\mathrm{tot}} = \sum_s \left(\hat{H}_A^{(s)} + \sum_{s>s'} \hat{U}_{ss'}(\hat{q}_s, \hat{q}_{s'}) \right) + \sum_s \sum_{j_s} \left[\frac{\hat{p}_{j_s}^2}{2m_{j_s}} + \frac{m_{j_s}\omega_{j_s}^2}{2} \left(\hat{x}_{j_s} - \frac{\alpha_{j_s} \hat{V}_s(\hat{q}_s)}{m_{j_s}\omega_{j_s}^2} \right)^2 \right], \quad (1)$$

where the Hamiltonian for the sth mode is defined as

$$\hat{H}_A^{(s)} = \frac{\hat{p}_s^2}{2m_s} + \hat{U}_s(\hat{q}_s) \quad (2)$$

with a mass m_s, a coordinate $\hat{q}_s$, and a momentum $\hat{p}_s$. The anharmonic potential for the sth mode is given by

$$\hat{U}_s(\hat{q}_s) = \frac{1}{2} m_s \omega_s^2 \hat{q}_s^2 + \frac{1}{3!} g_{s^3} \hat{q}_s^3, \quad (3)$$

where ω_s is the vibrational frequency and g_{s^3} denotes the cubic anharmonicity.

The interaction potential between the sth and s'th vibrational modes is formulated as

$$\hat{U}_{ss'}(\hat{q}_s, \hat{q}_{s'}) = g_{ss'} \hat{q}_s \hat{q}_{s'} + \frac{1}{6} \left(g_{s^2 s'} \hat{q}_s^2 \hat{q}_{s'} + g_{ss'^2} \hat{q}_s \hat{q}_{s'}^2 \right), \quad (4)$$

where $g_{ss'}$ denotes the second-order anharmonic coupling coefficient, while $g_{s^2 s'}$ and $g_{ss'^2}$ characterize the third-order contributions. Each oscillator in the sth bath, labeled by index j_s, is characterized by its momentum p_{j_s}, coordinate x_{j_s}, mass m_{j_s}, frequency ω_{j_s}, and coupling strength α_{j_s}. To preserve the system's translational invariance, a counter term is incorporated into each bath, as illustrated in Refs. 40 and 41.

While 2D spectroscopy has elucidated the roles of vibrational relaxation and dephasing as key mechanisms driving molecular motion,[42–53] incorporating these effects into theoretical models requires careful treatment of non-Markovian S–B interactions—particularly those of the linear–linear (LL)[41] and square–linear (SL) types[37–40]—as well as anharmonic mode–mode couplings. Accordingly, we describe the system component of the S–B interaction, $\hat{V}_s(\hat{q}_s)$, in terms of LL and SL contributions as

01 December 2025 21:12:15

Published under an exclusive license by AIP Publishing

$$\hat{V}_s(\hat{q}_s) \equiv \hat{V}_{\mathrm{LL}}^{(s)}\hat{q}_s + \frac{1}{2}\hat{V}_{\mathrm{SL}}^{(s)}\hat{q}_s^2, \tag{5}$$

where $V_{\mathrm{LL}}^{(s)}$ and $V_{\mathrm{SL}}^{(s)}$ denote the respective coupling strengths.[15,32]

The dynamics of the baths can be characterized via the SDFs and the inverse temperature $\beta = 1/k_{\mathrm{B}}T$, where k_{B} is Boltzmann's constant and T is the thermodynamic temperature. These quantities enter the theory through the symmetrized correlation function and the relaxation function, given, respectively, by $C_s(t) = \hbar\int_0^\infty \mathrm{d}\omega\, J_s(\omega)\coth(\beta\hbar\omega/2)\cos(\omega t)$ and $\Psi(t) = 2\int_0^\infty \mathrm{d}\omega\, J_s(\omega)\cos(\omega t)/\omega$, which are related via the fluctuation–dissipation theorem.[32,54] The SDF for the sth mode is defined as

$$J_s(\omega) = \sum_{j_s} \frac{\alpha_{j_s}^2}{2m_{j_s}\omega_{j_s}}\delta(\omega - \omega_{j_s}). \tag{6}$$

In general, SDFs can exhibit intricate structures.[35] However, the HEOM framework imposes limitations on the functional form of SDFs that can be accommodated.[16] In this work, we consider two representative forms:

(a) **Drude SDF**, widely employed in 2D spectral simulations[25–31] and supported by several source codes,[29,31] is expressed as

$$J_s^{\mathrm{D}}(\omega) = \frac{m_s\zeta_s^{\mathrm{D}}}{2\pi}\frac{(\gamma_s^{\mathrm{D}})^2\omega}{\omega^2 + (\gamma_s^{\mathrm{D}})^2}, \tag{7}$$

where ζ_s^{D} is the S–B coupling strength and γ_s^{D} characterizes the spectral width, which is inversely related to the vibrational dephasing time $\tau_s = 1/\gamma_s^{\mathrm{D}}$.

(b) **Brownian Oscillator (BO) + Drude SDF**, which incorporates both Drude and underdamped BO components,[55,56] is given by

$$J_s(\omega) = \frac{m_s\zeta_s^{\mathrm{B}}}{2\pi}\frac{(\gamma_s^{\mathrm{B}})^2(\omega_s^{\mathrm{B}})^2\omega}{[(\omega_s^{\mathrm{B}})^2 - \omega^2]^2 + (\gamma_s^{\mathrm{B}})^2\omega^2} + \frac{m_s\zeta_s^{\mathrm{D}}}{2\pi}\frac{(\gamma_s^{\mathrm{D}})^2\omega}{\omega^2 + (\gamma_s^{\mathrm{D}})^2}, \tag{8}$$

where ζ_s^{B} and γ_s^{B} denote the coupling strength and inverse correlation time of the BO bath, respectively, while ω_s^{B} represents its central frequency.[57–59] The BO component typically accounts for spectrally inactive silent modes that lie outside the observation window.

The dipole moment and polarizability operators are defined as

$$\hat{\mu} = \sum_s \mu_s\hat{q}_s + \sum_{s,s'}\mu_{ss'}\hat{q}_s\hat{q}_{s'} \tag{9}$$

and

$$\hat{\Pi} = \sum_s \Pi_s\hat{q}_s + \sum_{s,s'}\Pi_{ss'}\hat{q}_s\hat{q}_{s'}, \tag{10}$$

respectively, where μ_s and $\mu_{ss'}$ denote the linear and nonlinear components of the dipole moment, respectively, and Π_s and $\Pi_{ss'}$ denote the corresponding elements of the polarizability.

The vibrational modes interact via mechanical anharmonic coupling (MAHC), characterized by the coefficients $g_{s^2s'}$ and $g_{ss'^2}$, and electric anharmonic coupling (EAHC), described by the nonlinear dipole and polarizability terms $\mu_{ss'}$ and $\Pi_{ss'}$.[27]

B. Constructing the MAB model via the ML approach

The methodology developed herein is broadly applicable to molecular systems embedded in diverse environments, such as biomolecular assemblies,[60,61] solid-state matrices,[62] and solutions.[36] To provide a clear and quantitative demonstration of its performance, we focus on liquid water as a representative system.[63–66]

Water and aqueous solutions have been extensively characterized using a range of advanced spectroscopic techniques, including 2D IR,[2,3,67–71] 2D IR-Raman,[72–74] and 2D THz-Raman spectroscopy.[4,75–78] These experimental approaches have been complemented by MD simulations,[49–53] which yield detailed insights essential for the development and validation of theoretical models.

In addition, the HEOM framework incorporating the MAB models has been successfully employed to predict 2D Raman[34] and 2D IR-Raman[27,28] signals prior to their experimental realization. The framework also exhibits sufficient flexibility to reproduce experimentally measured 2D IR-Raman[29] and 2D THz-Raman spectra.[26,31] Furthermore, computational tools integrating quantum and classical methodologies for simulating 2D spectra have been developed and made publicly available,[29,31] thereby enabling rigorous validation of the theoretical approach.

The ML methodology employed in this study builds upon a previous study.[35] The main advance here is the adoption of a fixed functional form for the SDF, tailored for compatibility with the HEOM formalism. In contrast to earlier models constructed using atomic coordinates, the present framework utilizes normal mode coordinates within an optimization scheme that is inherently compatible with the HEOM formalism. This coordinate choice facilitates efficient optimization, eliminates rotational and librational contributions, and enables the treatment of each vibrational mode with independent anharmonic potentials.

While the earlier MAB model was developed to account for collective vibrational modes, including intermolecular ones, the current representation is rooted in a single-molecule perspective, marking a conceptual shift in modeling strategy.

We consider the intramolecular vibrational modes of a water molecule extracted from MD simulations. These modes are described in terms of the two O–H bond lengths and the H–O–H bond angle of the kth water molecule, defined as

$$r_1^k = \left|\mathbf{x}_{\mathrm{O}}^k - \mathbf{x}_{\mathrm{H}_1}^k\right|, \tag{11}$$

$$r_2^k = \left|\mathbf{x}_{\mathrm{O}}^k - \mathbf{x}_{\mathrm{H}_2}^k\right|, \tag{12}$$

and

$$\theta^k = \arccos\left(\frac{\left(\mathbf{x}_{\mathrm{O}}^k - \mathbf{x}_{\mathrm{H}_1}^k\right)\cdot\left(\mathbf{x}_{\mathrm{O}}^k - \mathbf{x}_{\mathrm{H}_2}^k\right)}{r_1 r_2}\right), \tag{13}$$

where $\mathbf{x}_{\mathrm{O}}$, $\mathbf{x}_{\mathrm{H}_1}$, and $\mathbf{x}_{\mathrm{H}_e}$ are the positions of the oxygen, the first, and the second hydrogen atoms, respectively, describing the intramolecular motion of the kth molecule.

01 December 2025 21:12:15

Published under an exclusive license by AIP Publishing

The MAB model presented in Eqs. (1)–(5) comprises three intramolecular vibrational modes of the water molecule: (1) asymmetric O–H stretching, (1′) symmetric O–H stretching, and (2) H–O–H bending. These modes are, respectively, expressed as

$$(1) \quad q_1^k = \frac{1}{2}\left(r_1^k - r_2^k\right),$$

$$(1') \quad q_{1'}^k = \frac{1}{2}\left(r_1^k + r_2^k - 2r_0\right),$$

and

$$(2) \quad q_2^k = \theta^k - \theta_0,$$

where r_0 is the equilibrium length of the OH bond and θ_0 is the equilibrium bending angle. The MAB model includes the anharmonic interactions between the modes. The thermal effects, including vibrational dephasing, are described as interactions between each mode and its harmonic bath.

To optimize the parameter set of the MAB model using MD trajectories, we employ a generative ML approach comprising the following steps: (i) MD trajectories q_j^k are generated for water molecules. (ii) For the kth molecule, the trajectory of q_j^k from time $t-1$ to t is simulated using the MAB model with a trial parameter set. (iii) A loss function at time t is evaluated to quantify the discrepancy between the reference MD trajectory from step (i) and

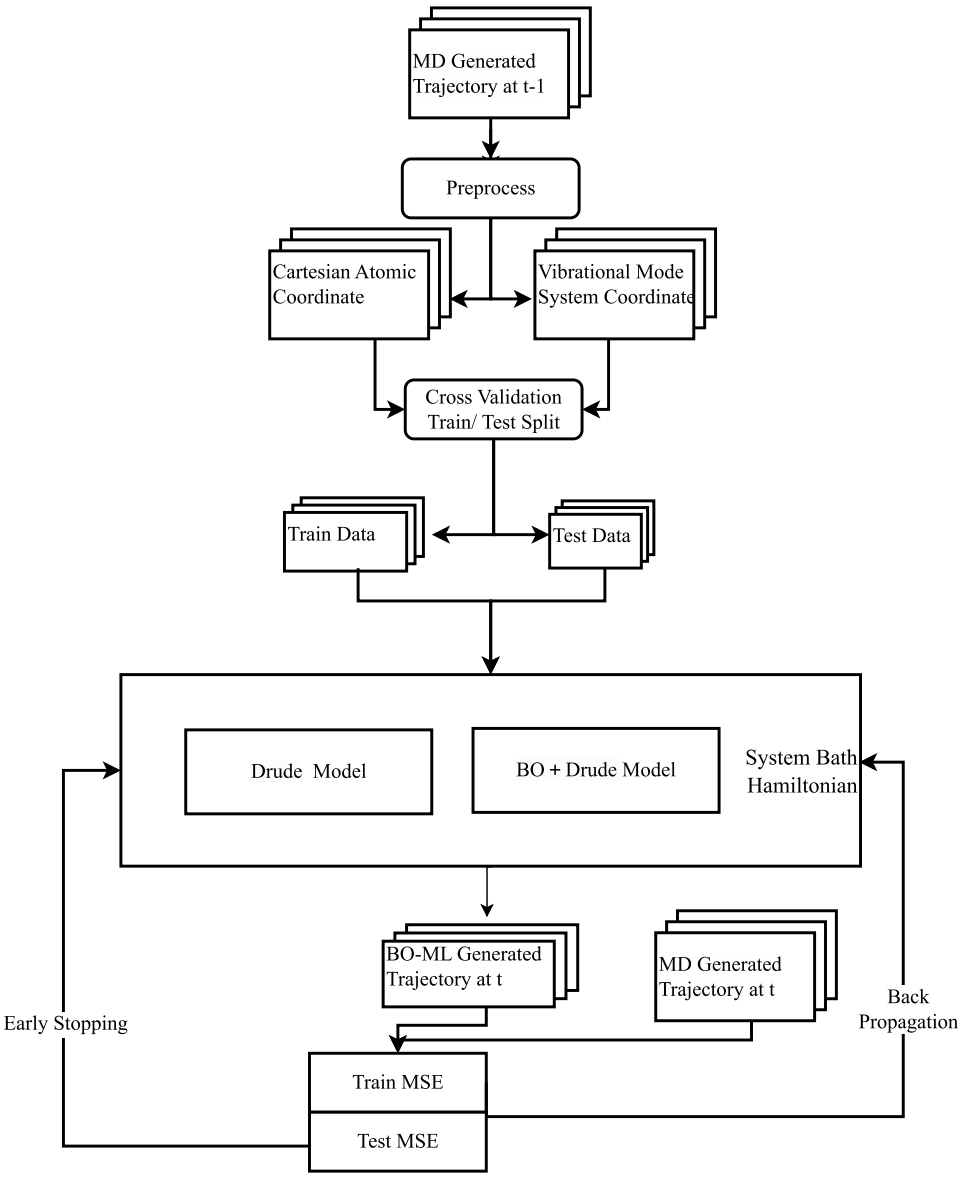

FIG. 1. Flow chart of the algorithm used to optimize the parameters of the MAB model based on atomic trajectories obtained from MD simulations.

01 December 2025 21:12:15

Published under an exclusive license by AIP Publishing

the ML-generated trajectory from step (ii). (iv) The loss is back-propagated to update the parameters of the MAB model, thereby iteratively enhancing its predictive accuracy. This procedure was applied to both case (a) in Eq. (7) and case (b) in Eq. (8).

More specifically, we analyze the trajectory set for the kth water molecule, represented as $\left(\mathbf{q}^k(t), \mathbf{p}^k(t)\right) \equiv \left(\{q_s^k(t)\}, \{p_s^k(t)\}\right)$, where s represents the vibrational modes. From MD simulations, we obtain a sequence of phase-space trajectories $\left(\mathbf{q}^k(t_0 + i\Delta t), \mathbf{p}^k(t_0 + i\Delta t)\right)$ sampled at time intervals Δt, with i satisfying $0 \le i \le N-1$, and N denoting the total number of time steps. Using the MAB model, we generate a corresponding sequence of predicted trajectories, denoted as $\left(\tilde{\mathbf{q}}^k(t_0 + i\Delta t), \tilde{\mathbf{p}}^k(t_0 + i\Delta t)\right)$. Within the ML framework, we optimize the parameters in Eqs. (1)–(5), along with the SDF parameters in Eq. (7) or Eq. (8), to reproduce the reference MD trajectories.

The thermal bath associated with the sth vibrational mode of the kth water molecule is modeled as a finite set of harmonic oscillators, each described by a coordinate x_{j_s}. The trajectory of this composite system is assumed to take the form[35]

$$\tilde{x}_{j_s}(t) = A_{j_s} \sin\left(\omega_{j_s} t + \phi_{j_s}\right), \tag{14}$$

where A_{j_s} and ϕ_{j_s} are the amplitude and phase of the j_sth bath oscillator, respectively. While ϕ_{j_s} is chosen randomly to prevent recursive motion, A_{j_s} are evaluated from Eq. (7) or Eq. (8) as learning parameters. For LL coupling, the bath parameters and the S–B interactions are expressed as a set of latent variables,

$$z_k = \{c_{j_s}^k\}, \tag{15}$$

where $c_{j_s}^k$ is defined as

$$c_{j_s}^k = \alpha_{js} V_{\mathrm{LL}}(q_s) A_{j_s}. \tag{16}$$

In addition, V_{SL} is learned as the ratio of these latent variables.

The trajectory at time $t_0 + i\Delta t$ can then be calculated using the MAB model,

$$\left(\tilde{\mathbf{q}}^k(t_0 + i\Delta t), \tilde{\mathbf{p}}^k(t_0 + i\Delta t)\right) = \hat{L}(\Delta t; z_k, \Sigma) \times \left(\tilde{\mathbf{q}}^k(t_0 + (i-1)\Delta t),\ \tilde{\mathbf{p}}^k(t_0 + (i-1)\Delta t)\right), \tag{17}$$

where $\left(\tilde{\mathbf{q}}^k(t), \tilde{\mathbf{p}}^k(t)\right)$ are the momentum and coordinate of the kth molecule, $\hat{L}(\Delta t; z_k, \Sigma)$ is the Liouvillian for Eqs. (1)–(5) with the discretized heat bath, and Σ represents the set of system and bath parameters.

We define the loss function as the Mean Squared Error (MSE) between the predicted and actual MD trajectories for the sth mode,

$$\mathrm{MSE}_{q_s} \equiv \frac{1}{N}\sum_{i=1}^{N}\left[\tilde{q}_s^k(t_i) - q_s^k(t_i)\right]^2. \tag{18}$$

Minimization of the loss functions corresponds to the optimization of the learning model parameters. These include the anharmonicity of the potential energy surfaces, anharmonic mode–mode couplings, coupling strengths for LL and SL interactions, and the SDF parameters associated with each vibrational mode. We further evaluated the descriptive efficiency of atomic vs normal mode coordinates by computing the MSE for each representation (see Appendix B). A schematic overview of the learning algorithm is provided in Fig. 1.

C. HEOM with BO+Drude SDF

The phase-space formulation of the HEOM, originally developed for the MAB system with the Drude SDF [case (a)], has been extended to quantum two-mode systems via the quantum hierarchical Fokker–Planck equations (QHFPEs)[28,29] and to classical three-mode systems via the classical hierarchical Fokker–Planck equations (CHFPEs).[27,30] The source codes for both implementations are publicly available.[29,31]

For case (b), involving the BO+Drude SDF, the hierarchy space requires further extension. This extended framework has previously been employed to simulate 2D electronic spectra (2DES) of electron transfer systems.[56] In the present study, we apply this approach to the eigenstate representation of the reduced density operator of the MAB system, $\hat{\rho}(t)$, thereby enabling an explicit quantum treatment of intramolecular vibrational modes. For case (a), calculations can be performed without any extension by deactivating the BO bath within the same BO+Drude HEOM framework. To apply this framework, the system must be described in terms of the eigenenergy states of the system S. In HEOM described in this representation, unlike QHFPE, the counter term in Eq. (1) must be explicitly included in the system Hamiltonian as

$$\hat{H}_S' = \sum_s \left(\hat{H}_A^{(s)} + \Lambda^{(s)}\hat{V}_s^2\right) + \sum_{s>s'}\hat{U}_{ss'} \tag{19}$$

with $\Lambda^{(s)} = \sum_{j_s}\alpha_{j_s}^2/2m_{j_s}\omega_{j_s}^2$. For a given SDF, the counter term is evaluated as $\Lambda^{(s)} = \int_0^\infty d\omega J_s(\omega)/\omega$.[41] For the BO+Drude case, this is evaluated as

$$\Lambda^{(s)} = \frac{m_s\zeta_s^{\mathrm{B}}\gamma_s^{\mathrm{B}}}{4} + \frac{m_s\zeta_s^{\mathrm{D}}\gamma_s^{\mathrm{D}}}{2}. \tag{20}$$

The Drude-only case is obtained by setting $\zeta_s^{\mathrm{B}} = 0$.

We defined $\nu_{-2}^s \equiv \gamma_s^{\mathrm{B}} + i\delta_s^{\mathrm{B}}$ and $\nu_{-1}^s \equiv \gamma_s^{\mathrm{B}} - i\delta_s^{\mathrm{B}}$ with $\delta_s^{\mathrm{B}} = \sqrt{(\omega_s^{\mathrm{B}})^2 - (\gamma_s^{\mathrm{B}})^2/4}$ and $\nu_0^s \equiv \gamma_s^D$. We then introduce the Padé approximation to express the thermal effects as ν_k^s, where $k = \{1, 2, \ldots, K_s\}$. We introduce the hyperoperators $\hat{A}^\times\hat{B} \equiv \hat{A}\hat{B} - \hat{B}\hat{A}$ and $\hat{A}^\circ\hat{B} \equiv \hat{A}\hat{B} + \hat{B}\hat{A}$, defined for arbitrary operators $\hat{A}$ and $\hat{B}$. The HEOM for BO+Drude SDF is then expressed as follows:[56]

$$\frac{d}{dt}\hat{\rho}_{\{\mathbf{n}_s\}} = -\left[\frac{i}{\hbar}\hat{H}_S'^\times + \sum_s\sum_{k=-2}^{K_s}\left(n_k^s\nu_k^s\right)\right]\hat{\rho}_{\{\mathbf{n}_s\}} - i\sum_s\sum_{k=-2}^{K_s} n_k^s\hat{\Theta}_k^s\hat{\rho}_{\{\mathbf{n}_s-\mathbf{e}_s^k\}} - i\sum_s\sum_{k=-2}^{K_s}\hat{V}_s^\times\hat{\rho}_{\{\mathbf{n}_s+\mathbf{e}_s^k\}}. \tag{21}$$

The hierarchy elements are indexed by the set $\{\mathbf{n}_s\} \equiv (\mathbf{n}_1, \mathbf{n}_{1'}, \mathbf{n}_2)$, where each $\mathbf{n}_s$ is a multi-index defined as $\mathbf{n}_s = (n_{-2}^s, n_{-1}^s, n_0^s, n_1^s, \ldots, n_{K_s}^s)$ for the three-mode case. All $\hat{\rho}_{\{\mathbf{n}_s\}}(t)$ with any negative index $n_k^s < 0$ are set to zero. The notation

01 December 2025 21:12:15

Published under an exclusive license by AIP Publishing

$\{\mathbf{n}_s \pm \mathbf{e}_s^k\}$ indicates an increment or decrement of the kth component of $\mathbf{n}_s$, where $\mathbf{e}_s^k$ is the unit vector corresponding to the kth frequency component in the sth bath. The operators are defined as

$$\hat{\Theta}_{-2}^{(s)} = \frac{m_s\zeta_s^{\mathrm{B}}\gamma_s^{\mathrm{B}}(\omega_s^{\mathrm{B}})^2}{8\hbar\delta_s^{\mathrm{B}}}\left\{i\hat{V}_s^{\circ} - \bar{A}_s^{+}\hat{V}_s^{\times}\right\}, \tag{22}$$

$$\hat{\Theta}_{-1}^{(s)} = \frac{m_s\zeta_s^{\mathrm{B}}\gamma_s^{\mathrm{B}}(\omega_s^{\mathrm{B}})^2}{8\hbar\delta_s^{\mathrm{B}}}\left\{-i\hat{V}_s^{\circ} + \bar{A}_s^{-}\hat{V}_s^{\times}\right\}, \tag{23}$$

$$\hat{\Theta}_{0}^{(s)} = \frac{m_s\zeta_s^{\mathrm{D}}\gamma_s^{\mathrm{D}}}{4\hbar\beta}\left(1 + \sum_{k=1}^{K_s}\frac{2\eta_k^s\gamma_s^2}{(\gamma_s^{\mathrm{D}})^2 - \nu_k^{s\,2}}\right)\hat{V}_s^{\times}, \tag{24}$$

and

$$\hat{\Theta}_{k>0}^{(s)} = -\frac{B_s^k}{\hbar}\hat{V}_s^{\times}, \tag{25}$$

where the parameters η_k^s and ν_k^s denote the Padé-approximated thermal coupling intensity and frequency,[79] and we introduce

$$\bar{A}_s^{+} = \frac{2}{\beta\hbar(\delta_s^{\mathrm{B}} - i\gamma_s^{\mathrm{B}}/2)}\left(1 + \sum_{k=1}^{K}\frac{2\eta_k^s(\delta_s^{\mathrm{B}} - i\gamma_s^{\mathrm{B}}/2)}{(\delta_s^{\mathrm{B}} - i\gamma_s^{\mathrm{B}})^2 + (\nu_k^s)^2}\right), \tag{26}$$

$$\bar{A}_s^{-} = \frac{2}{\beta\hbar(\delta_s^{\mathrm{B}} + i\gamma_s^{\mathrm{B}}/2)}\left(1 + \sum_{k=1}^{K}\frac{2\eta_k^s(\delta_s^{\mathrm{B}} + i\gamma_s^{\mathrm{B}}/2)}{(\delta_s^{\mathrm{B}} + i\gamma_s^{\mathrm{B}})^2 + (\nu_k^s)^2}\right), \tag{27}$$

and

$$B_s^k = \left\{\frac{m_s\zeta_s^{\mathrm{D}}(\gamma_s^{\mathrm{D}})^2}{\beta\hbar}\frac{\nu_k}{(\gamma_s^{\mathrm{D}})^2 - \nu_k^2} + \frac{m_s\zeta_s^{\mathrm{B}}(\gamma_s^{\mathrm{B}})^2(\omega_s^{\mathrm{B}})^2}{\beta\hbar}\frac{\nu_k}{\left[(\omega_s^{\mathrm{B}})^2 + \nu_k^2\right]^2 - (\gamma_s^{\mathrm{B}})^2\nu_k^2}\right\}. \tag{28}$$

D. Linear absorption spectra

The infrared absorption spectrum is calculated from[27,28]

$$\alpha(\omega) = \omega\,\mathrm{Im}\int_0^{\infty} dt\, e^{i\omega t}\, R^{(1)}(t), \tag{29}$$

where the first-order response function of dipole moment is defined as $R^{(1)}(t) = i\langle[\hat{\mu}(t), \hat{\mu}(0)]\rangle/\hbar$. We can rewrite the response function as[16,32]

$$R^{(1)}(t) = \frac{i}{\hbar}\,\mathrm{Tr}\{\hat{\mu}\hat{\mathcal{G}}(t)\hat{\mu}^{\times}\hat{\rho}^{eq}\}, \tag{30}$$

where $\hat{\mathcal{G}}(t)$ represents the Green's function associated with Eq. (21), while $\hat{\rho}^{eq}$ represents the equilibrium density operator, derived from the steady-state solution of the HEOM. To evaluate $R^{(1)}(t)$, we solve the HEOM starting from the initial state at $t = 0$, given as $\hat{\mu}^{\times}\hat{\rho}^{eq}$. The solution obtained at time t is referred to as $\hat{\rho}'(t)$. The response function is then calculated as the expectation value, $R^{(1)}(t) = i\mathrm{tr}\{\hat{\mu}\hat{\rho}'(t)\}/\hbar$.

Using parameters learned via the MAB model, we incorporate the HEOM formalism to compute linear-response spectra without resorting to ad hoc fitting to experimental or simulated data. Training on MD trajectories ensures consistency with microscopic dynamics, thereby mitigating ambiguities inherent in spectrum-based fitting.

For the Drude case, both the quantum hierarchical Fokker–Planck equation (QHFPE)[28,29] and the classical hierarchical Fokker–Planck equation (CHFPE)[26,27,30,31] have been developed. In the BO+Drude case, the HEOM code capable of simulating nonlinear vibrational spectroscopy for a single-mode system has been developed.[56] In both frameworks, computational programs capable of simulating 2D vibrational spectra of quantum systems with three coupled modes are currently under development.

III. APPLICATION TO WATER

A. Collective vs single-molecule representation

In previous studies, the parameter values of the MAB model employed in HEOM were tuned to reproduce the peak positions and spectral features of the 2D spectrum obtained from MD simulations.[25–31] Within this framework, the coordinates $q_s(t)$ assigned to each mode—including intermolecular ones—are interpreted as representing collective motions. These coordinates are not directly extracted from atomic trajectories but are instead inferred from their time correlation functions via the dipole response. In contrast, the ML approach presented in this study builds upon a single-molecule perspective[35] and offers a fundamentally different physical interpretation of $q_s(t)$. Thus, the physical interpretation of mode coupling becomes more transparent, while the *inhomogeneous broadening of spectral line shapes is significantly reduced.*

Nevertheless, to ensure a smooth transition to the HEOM framework, we modified the previous ML approach,[35] in which the stretching and bending motions of surrounding molecules were treated as bath components, leading to peaks at the corresponding frequencies in the SDF. Thus, in the present study, by constraining the SDF to either a Drude or BO+Drude form, we guided the learning process to interpret these vibrational modes not as bath components, but as contributors to inter-mode coupling.

B. Details of the ML approach

We validate our methodology by optimizing the parameters of the MAB model for water, yielding a description suitable for computing diverse spectral profiles. MD trajectories for ML were generated using a system consisting of 392 water molecules confined within a cubic box measuring 2.3 nm per side. The system was maintained at a temperature of 300 K. Simulations were performed for 50 ps using GROMACS,[80] with water molecules represented by the Ferguson potential model[81] with the Amber03 force field. More detailed explanations about the potential function of each MD simulation can be found in Appendix A.

The resulting trajectories were transformed into normal mode coordinates corresponding to intramolecular vibrations (see Appendix B). We then trained models for two cases: (a) the Drude SDF case and (b) the BO+Drude SDF case. For each training and

01 December 2025 21:12:15

Published under an exclusive license by AIP Publishing

testing split, early stopping was applied with a patience threshold of 300 epochs. Optimization was terminated when the test loss did not improve for 300 consecutive epochs (see Appendix C). This strategy reduced overfitting while ensuring a consistent stopping criterion.

In the evaluation of mode coupling, each coupling coefficient was calculated twice because the trajectories of the two modes were optimized independently. In particular, the coefficient was computed once during the optimization of mode s and once during the optimization of mode s'. Although these two estimates were obtained from separate optimization processes, they correspond to the same physical interaction. Therefore, we adopt the averaged values for three types of mode coupling: linear–linear, square–linear, and linear–squared. These are defined, respectively, as $\bar{g}_{s's} = (g_{ss'} + g_{s's})/2$, $\bar{g}_{s^2s'} = (g_{s^2s'} + g_{s's^2})/2$, and $\bar{g}_{ss'^2} = (g_{ss'^2} + g_{s'^2s})/2$.

To implement early stopping, we employed Time Step Cross-Validation (TSCV), a method designed to preserve the temporal continuity of the system's dynamics. This strategy enables systematic evaluation of how various optimization conditions influence model accuracy, including molecular sampling schemes derived from MD trajectories, time step resolutions, and model flexibility or adjustability. In the TSCV, each fold was constructed by training on the initial 4000 fs of the trajectory and testing on the subsequent 1000 fs (i.e., the next 1000 time steps). This procedure was repeated to generate four non-overlapping train–test splits. Within this framework, the same molecules interact in the same bath environment up to 4 ps, aligning well with the single-molecule perspective. Alternative cross-validation strategies were assessed in Appendix D, yet TSCV offered a more consistent and physically grounded basis for spectral simulation.

During the development of the learning framework, the selection of initial values proved to be a decisive factor influencing the optimization results. In non-convex landscapes, poor initialization can trap algorithms near local optima or saddle points. This directly impacts the S–B trade-off. For example, prior ML research[35] reported substantially weaker S–B coupling compared to results obtained using the collective coordinate framework. Such a discrepancy is anticipated: both that study and the present work rely on single-molecule trajectories for ML, which inherently reflect more localized and weaker bath environments than those revealed through spectral analysis of collective coordinates. Furthermore, when the system model possesses sufficient flexibility, the optimization process may allocate residual variance to the system rather than the bath, further diminishing the apparent S–B coupling strength. The discrepancy was traced to initial parameter values that constrained the system to a local minimum associated with an elevated harmonic potential. To mitigate this, initial values for the system potential parameters were selected to correspond to infrared stretch and bend peaks, providing physically motivated starting points for optimization.

Guided by this rationale, the training procedure was structured into two sequential stages. In the first stage, the system potential parameters and bath terms were jointly optimized to establish a consistent baseline representation of the vibrational modes and their surrounding environment. Upon convergence, these parameters were held fixed. In the second stage, we refined the higher-order interactions, focusing specifically on the mode–mode coupling terms and the anharmonicity of the potential. This staged protocol reflects the logic of the initialization: by constraining the baseline potential and bath response, the subsequent estimation of mode–mode couplings is less susceptible to spurious minima and yields parameters that more faithfully capture the intrinsic physical correlations among vibrational modes.

For ML, model training was performed using Python 3.9.18 in conjunction with TensorFlow 2.15 and CUDA 12.2. All computations were executed on a system equipped with an Intel Core i9-13900H CPU and an NVIDIA GeForce RTX 4070 GPU. Our approach builds on previously developed algorithms for constructing MAB models via ML.[35] We minimize the MSE using the Adam optimizer with an initial learning rate of 0.5. Validation MSE is monitored, and early stopping is applied: if no improvement is observed for 300 epochs, the learning rate is reduced to 0.001 and training continues. If a second plateau occurs, training is terminated. Each batch comprises 25 molecules and 1000 time steps. We use fourfold cross-validation per vibrational mode. On our hardware, onefold for a single mode takes approximately 2–4 h, so all three modes across fourfolds take roughly 24–48 h.

C. Optimized parameter set

We optimized the parameters associated with the intramolecular vibrational modes under two distinct frameworks: (a) the Drude SDF and (b) the BO+Drude SDF. The computational protocol employed to generate the absorption spectra is schematically depicted in Fig. 2.

Previous studies[35] have demonstrated that the SDF obtained via ML in the single-molecule framework is significantly more intricate than the Drude SDF, displaying distinct peaks corresponding to each intermolecular and intramolecular vibrational mode. Notably, the contribution of each intramolecular three-mode component, when modeled as a bath, can be effectively captured by the Drude representation, provided that strong mode–mode coupling is adequately incorporated. In contrast, low-frequency intermolecular vibrations are not sufficiently described by the Drude bath alone. To remedy this limitation, we incorporated a BO mode to account for relaxation pathways into the intermolecular vibrational manifold. This hybrid BO+Drude bath model was found to yield a reduced learning loss relative to the Drude-only counterpart, thereby offering a more accurate representation of the S–B interaction.

Several studies have been conducted using the MAB model for the collective mode of water in the Drude framework.[25–31] In these investigations, the model parameters for water were selected to reproduce the peak positions and spectral profiles observed in 1D and 2D spectra obtained directly from MD simulations. In the current study, these parameters were determined using ML based on atomic trajectories obtained from the MD.

Accordingly, the parameters of the MAB model introduced herein are defined with respect to single-molecule coordinates and are, therefore, not directly comparable to prior results formulated in terms of collective coordinates. It is also noteworthy that earlier modeling efforts have predominantly targeted optical observables—such as polarization and its temporal derivative—without explicitly resolving the underlying molecular coordinates. In contrast, the present approach affords a more granular depiction of MD at the microscopic level. Importantly, it enables the identification and characterization of spectroscopically inactive (dark) states that are inaccessible via conventional optical probes.

01 December 2025 21:12:15

Published under an exclusive license by AIP Publishing

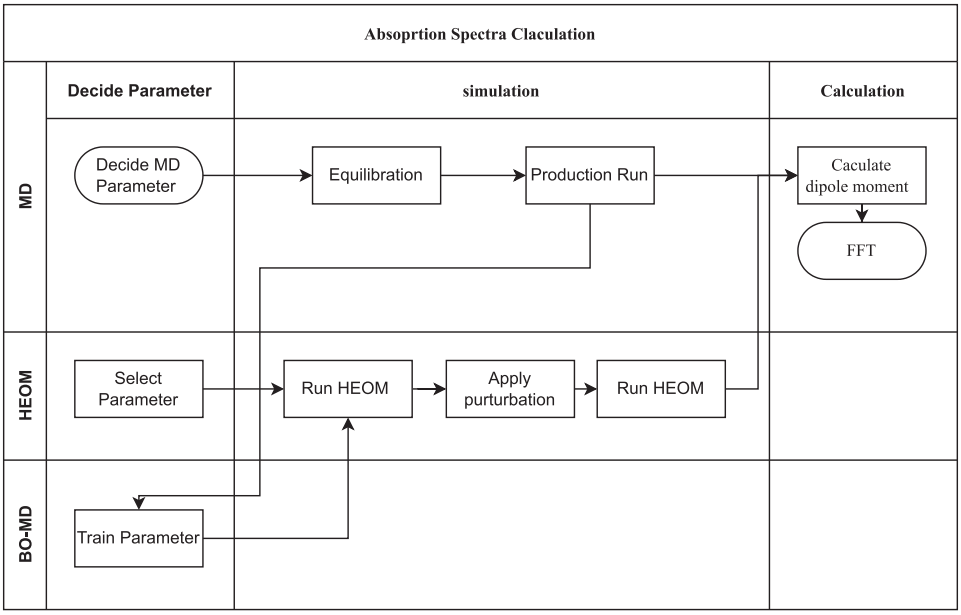

FIG. 2. Schematic workflow for spectral calculation. Starting from MD trajectories, we first train the bath parameters and mode–mode coupling strength. The trained parameters are then passed to HEOM propagation, and the Fourier transform yields the final IR absorption spectrum.

Despite the methodological disparities, we endeavor to compare the present results with model parameters reported in prior studies. Such a comparison facilitates a critical examination of the differences between collective and molecular coordinate representations, with particular emphasis on the respective roles of vibrational mode coupling and environmental bath interactions. The non-Markovian nature of the bath is essential, as the correlation time of the bath noise determines the vibrational dephasing time.[15,25,39] In the high-frequency regime—typified by intramolecular vibrations—the impact of LL coupling on the spectral profile is negligible relative to that of SL coupling.[39] Accordingly, we begin by considering a simplified scenario in which the LL S-B coupling is omitted.

1. Drude bath with SL interaction

To enable direct comparison with previous studies employing collective modes[27–29] and to facilitate the computation of the 2D spectrum using the quantum simulation code currently under development, we adopted the same formatting conventions as those used in Refs. 30 and 31. Accordingly, the scaling of quantities follows $\tilde{\zeta}_s^{\mathrm{D}} \equiv \zeta_s^{\mathrm{D}}(\omega_0/\omega_s)^2$, with $\omega_0 = 4000\ \mathrm{cm}^{-1}$, and γ_s^{D} is reported as $\gamma_s^{\mathrm{D}}/\omega_0$. For mode–mode coupling, the parameters are normalized as $\tilde{g}_{s^3} = \bar{g}_{s^3}(\omega_0/\omega_s)^3$, $\tilde{g}_{s's} = \bar{g}_{s's}(\omega_0/\omega_s)(\omega_0/\omega s')$, $\tilde{g}_{s^2s'} = \bar{g}_{s^2s'}(\omega_0/\omega_s)^2(\omega_0/\omega s')$, and $\tilde{g}_{ss'^2} = \bar{g}_{ss'^2}(\omega_0/\omega_s)(\omega_0/\omega s')^2$.

The parameters of the MAB model for the Drude bath with SL interaction derived via the ML approach are compiled in Tables I and II, expressed as functions of molecular coordinates: These tables correspond to Tables II–IV, respectively, in Ref. 30.

Table I reveals notably large anharmonicity, which is primarily attributed to the single molecular picture employed in the present modeling for the ML algorithm's development. While previous model parameters evaluated from 2D spectra could not distinguish the anharmonicity between modes (1) and (1′), and thus assigned them identical values, our analysis shows that the anharmonicity of mode (1′) is ~34 times greater than that of mode (1). We also examined alternative MD force fields, including the SPC/E water model, and found that the resulting anharmonicity and mode-coupling parameters were highly sensitive to the choice of force field. The analysis of different potentials will be presented to demonstrate

TABLE I. Optimized parameters of the MAB model, trained using the Ferguson potential with incorporated Drude SDF and SL interaction, are presented for the following vibrational modes: (1) asymmetric stretch, (1′) symmetric stretch, and (2) bending. Here, $\tilde{\zeta}_s^{\mathrm{D}}$ denotes the normalized S–B coupling strength, γ_s^{D} denotes the inverse correlation time of the bath fluctuations, $V_{\mathrm{SL}}^{(s)}$ and $V_{\mathrm{LL}}^{(s)}$ denote the SL and LL interactions, and $\tilde{g}_{s^3}$ is the cubic anharmonicity for the s vibrational mode, respectively.

ω_s	(cm^{-1})	$\gamma_s^{\mathrm{D}}/\omega_0$	$\tilde{\zeta}_s^{\mathrm{D}}$	$\tilde{V}_{LL}^{(s)}$	$\tilde{V}_{SL}^{(s)}$	$\tilde{g}_{s^3}$
1	3513	2.42×10^{-2}	3.42×10^{-2}	0	1.00	3.64×10^{-3}
1′	3413	2.42×10^{-2}	3.43×10^{-2}	0	1.00	0.125
2	1636	1.73×10^{-3}	1.79×10^{4}	0	1.00	2.895

TABLE II. Optimized mode–mode coupling parameters of the MAB model trained from the Ferguson potential with the Drude SDF and SL interaction for (1) asymmetric stretch, (1′) symmetric stretch, and (2) bending modes.

$s - s'$	$\tilde{g}_{ss'}$	$\tilde{g}_{s^2s'}$	$\tilde{g}_{ss'^2}$
1–1′	3.78×10^{-2}	1.11×10^{-2}	0.192
1–2	5.15×10^{-2}	7.74×10^{-2}	5.13×10^{-2}
1′–2	−2.282	9.15×10^{-2}	0.172

01 December 2025 21:12:15

Published under an exclusive license by AIP Publishing

TABLE III. Optimized parameters of the MAB model trained from the Ferguson potential with the Drude SDF and LL+SL interaction for (1) asymmetric stretching, (1′) symmetric stretching, and (2) bending modes. Here, $\tilde{\zeta}_s^{\mathrm{D}}$ denotes the normalized S–B coupling strength, γ_s^{D} denotes the inverse correlation time of the bath fluctuations, $V_{\mathrm{SL}}^{(s)}$ and $V_{\mathrm{LL}}^{(s)}$ denote the SL and LL interactions, and $\tilde{g}_{s^3}$ is the cubic anharmonicity for the s vibrational mode, respectively.

ω_s (cm^{-1})		$\gamma_s^{\mathrm{D}}/\omega_0$	$\tilde{\zeta}_s^{\mathrm{D}}$	$\tilde{V}_{LL}^{(s)}$	$\tilde{V}_{SL}^{(s)}$	$\tilde{g}_{s^3}$
1	3513	2.41×10^{-2}	1.97×10^{-2}	3.31×10^{-1}	1.00	1.08×10^{-2}
1′	3413	2.42×10^{-2}	3.31×10^{-2}	3.26×10^{-1}	1.00	0.115
2	1636	1.80×10^{-3}	1.71×10^{4}	2.58×10^{-1}	1.00	2.927

the ML algorithm employed in this study, serving as an illustrative example in the forthcoming publication.

Although the absolute values differ, the S–B parameters exhibit consistent trends across vibrational modes—except for the S–B coupling strength of the bending mode, which may reflect the limited angular variation permitted by the MD force field. In contrast, the deviation observed in the stretching mode may be attributed to hydrogen bonding and could reflect intrinsic characteristics of the microscopic water structure.

Table II presents the results for mode–mode coupling. Compared to the collective coordinate results (Tables II and III of Ref. 30), the magnitude of the anharmonic coupling is estimated to be different. The observed difference arises mainly from the adoption of an OH stretching potential that captures the differing degrees of anharmonicity between the two vibrational modes.

For linear absorption spectra, where the influence of anharmonicity and mode coupling is minimal, the choice of force field has only a minor impact. In contrast, anharmonicity plays a critical role in simulating 2D vibrational spectra, necessitating the use of accurate force fields. Given the pronounced quantum nature of intramolecular vibrations, quantum MD trajectories—such as those provided by POLI2VS[82] and MB-POL[83–85]—are preferable whenever available.

TABLE IV. Optimized mode–mode coupling strength of the MAB model trained from the Ferguson potential with the Drude SDF and LL+SL interaction for (1) asymmetric stretch, (1′) symmetric stretch, and (2) bending modes.

s − s′	$\tilde{g}_{ss'}$	$\tilde{g}_{s^2s'}$	$\tilde{g}_{ss'^2}$
1 − 1′	-1.21×10^{-2}	1.09×10^{-2}	0.199
1–2	-2.10×10^{-2}	7.96×10^{-2}	8.17×10^{-2}
1′ − 2	−2.295	7.77×10^{-2}	0.224

2. Drude bath with LL+SL interaction

The results incorporating LL+SL interactions are summarized in Tables III and IV. A comparison between Tables I and III reveals that, even with the inclusion of V_{LL} in the optimization, its overall contribution remains relatively minor. Accordingly, variations in other bath parameters are also limited.

We then examine the differences in mode coupling parameters listed in Tables II and IV. As with the bath parameters, the distinction between SL and LL+SL coupling remains marginal. In both cases, the strong couplings are observed for $\tilde{g}_{ss'}$ with $s = 1$ and $s' = 1$ and 1′ and 2. The second is due to the shared symmetry between the bending mode and the symmetric stretch mode, which facilitates vibrational interaction.

Regarding anharmonic coupling, the parameter $\tilde{g}_{ss'^2}$ is notably large when 1′ and $s' = 2$, reflecting the near-resonance between the overtone of the bending mode and the fundamental frequency of the stretch mode. However, the difference between the 1–2 and 1′–2 couplings is less pronounced than in previous studies.[30]

3. BO+Drude bath with SL interaction

The results for BO+Drude SDF with SL interaction are presented below. In this framework, the overdamped Drude SDF describes the relaxation of intramolecular modes, while the underdamped BO SDF represents the interactions with low-frequency intermolecular modes, including libration and hydrogen-bond translation. The inclusion of BO baths was guided by insights from

TABLE V. Optimized parameters of the MAB model trained from the Ferguson potential with BO+Drude SDF and SL interaction for (1) asymmetric stretching, (1′) symmetric stretching, and (2) bending modes. Here, $\tilde{\zeta}_s^{\mathrm{D}}$ denotes the normalized S–B coupling strength, γ_s^{D} denotes the inverse correlation time of the bath fluctuations for the Drude mode, and $\tilde{\zeta}_s^{\mathrm{B}}$ and γ_s^{B} are those for the BO mode. The central frequency of the BO mode is expressed as ω_s^{B}, $V_{\mathrm{SL}}^{(s)}$ and $V_{\mathrm{LL}}^{(s)}$ denote the SL and LL interactions, respectively, and $\tilde{g}_{s^3}$ is the cubic anharmonicity for the s vibrational mode.

ω_s (cm^{-1})		$\gamma_s^{\mathrm{D}}/\omega_0$	$\tilde{\zeta}_s^{\mathrm{D}}$	$\gamma_s^{\mathrm{B}}/\omega_0$	$\tilde{\zeta}_s^{\mathrm{B}}$	$\omega_s^{\mathrm{B}}/\omega_0$	$\tilde{V}_{\mathrm{LL}}^{(s)}$	$\tilde{V}_{\mathrm{SL}}^{(s)}$	$\tilde{g}_{s^3}$
1	3513	2.42×10^{-2}	2.01×10^{-2}	6.99×10^{-5}	1.37×10^{3}	8.95×10^{-3}	0	1.00	9.44×10^{-3}
1′	3413	2.42×10^{-2}	2.10×10^{-2}	9.21×10^{-5}	1.22×10^{3}	9.52×10^{-3}	0	1.00	0.127
2	1636	2.47×10^{-3}	6.65×10^{3}	8.21×10^{-3}	1.22×10^{3}	5.35×10^{-2}	0	1.00	1.662

01 December 2025 21:12:15

Published under an exclusive license by AIP Publishing

TABLE VI. Optimized mode–mode coupling parameters of the MAB model trained from the Ferguson potential with the BO+Drude SDF and SL interaction for (1) asymmetric stretch, (1′) symmetric stretch, and (2) bending modes.

s − s′	$\tilde{g}_{ss'}$	$\tilde{g}_{s^2s'}$	$\tilde{g}_{ss'^2}$
1 − 1′	3.03×10^{-2}	1.35×10^{-2}	0.204
1–2	-3.32×10^{-2}	5.66×10^{-2}	-6.02×10^{-2}
1′–2	−2.259	5.36×10^{-2}	0.115

TABLE VIII. Optimized mode–mode coupling parameters of the MAB model trained from the Ferguson potential with a more sensitive anharmonicity setting with the BO+Drude SDF and LL+SL interaction for (1) asymmetric stretch, (1′) symmetric stretch, and (2) bending modes.

s − s′	$\tilde{g}_{ss'}$	$\tilde{g}_{s^2s'}$	$\tilde{g}_{ss'^2}$
1 − 1′	5.23×10^{-3}	1.05×10^{-2}	0.204
1–2	-5.71×10^{-2}	7.21×10^{-2}	-4.84×10^{-2}
1′–2	−2.322	7.05×10^{-2}	4.56×10^{-2}

previous studies.[35] Incorporating BO modes was found to enhance learning efficiency relative to the Drude SDF alone.

For consistency with the collective coordinate representation, the BO parameters were normalized according to $\tilde{\zeta}_s^{\mathrm{B}} \equiv \zeta_s^{\mathrm{B}}(\omega_0/\omega_s)^2$, with γ_s^{B} and ω_s^{B} reported as $\gamma_s^{\mathrm{B}}/\omega_0$ and $\omega_s^{\mathrm{B}}/\omega_0$, respectively.

Table V summarizes the bath parameters and the potential anharmonicity as evaluated by ML. Although the inclusion of BO modes does not alter the correlation time of the Drude mode, it leads to a reduction in its coupling strength. In contrast, the coupling strength associated with the BO modes is substantially larger, suggesting an overestimation of the interaction between intramolecular and intermolecular vibrational modes. This likely stems from the BO–SDF framework assuming bilinear interactions, whereas such couplings are inherently anharmonic, leading to higher-order effects typical of strong BO coupling.

Table VI presents the evaluated mode coupling parameters. These values remain largely unchanged despite changes in the bath configuration, indicating that mode coupling, as a mechanical interaction, can be treated independently of the thermal bath configuration.

4. BO+Drude bath with LL+SL interaction

We finally present the BO+Drude SDF results incorporating both LL and SL interactions. The results are shown in Tables VII and VIII. As in the Drude-only case, inclusion of LL coupling results in minimal changes to bath parameters and mode coupling strengths relative to the SL-only optimization.

Within the MAB framework, the addition of LL coupling does not modify the optical profile of high-frequency intramolecular modes relative to the SL-only case, indicating that its exclusion during model parameterization may be justified.[39] Nonetheless, improved ML efficiency would enable seamless incorporation of V_{LL} into the training process.

The ML results described above faithfully reproduce the behavior of the original MD trajectories. Consequently, when constructing models for 2D spectroscopic simulations, it is essential to utilize MD trajectories generated with a highly descriptive force field.

D. Linear absorption spectra

Based on the obtained model parameters, the linear absorption spectrum was computed according to the scheme described in Sec. II D. While a complete validation of this approach requires calculation of the 2D vibrational spectrum, as a preliminary step, it is instructive to assess the reproducibility of the single-mode linear absorption spectrum. In this regime, effects such as mode coupling and anharmonicity are minimal, and multi-mode calculations yield only marginal differences. Nonetheless, this analysis remains effective for probing the influence of thermal baths, in particular, the BO+Drude case.

To evaluate Eq. (30), we integrate the HEOM in Eq. (21). The calculations were implemented in Python using NumPy 1.26.3 and Numba 0.60.0. Time evolution of HEOM was investigated via the fourth-order Runge–Kutta method.

In Fig. 3, the linear absorption spectra for the SL interaction are shown for (a) the Drude case and (b) the BO+Drude case. The corresponding parameter values are listed in Tables I and V. For comparison, each figure also includes the absorption spectrum obtained from MD simulations using the Ferguson potential model, in which the Cartesian coordinate components of the dipole moment for each molecule were evaluated from the MD trajectory, the corresponding autocorrelation functions were then calculated and averaged, and a Fourier transform was subsequently performed to obtain the absorption spectrum.

In Fig. 3(a), the results modeled by ML clearly distinguish between symmetric and antisymmetric vibrational modes, in contrast to the peaks directly obtained from MD trajectories. The peak predicted by the model appears sharper than that in the MD spectrum, as the model is based on a single-molecule picture and, thus, incorporates the effects of inhomogeneous broadening to a lesser extent. The BO+Drude result is presented in

TABLE VII. Optimized parameters of the MAB model trained from the Ferguson potential with BO+Drude SDF and LL+SL interaction for (1) asymmetric stretching, (1′) symmetric stretching, and (2) bending modes. The remaining parameters are as in Table V.

ω_s	(cm^{-1})	$\gamma_s^{\mathrm{D}}/\omega_0$	$\tilde{\zeta}_s^{\mathrm{D}}$	$\gamma_s^{\mathrm{B}}/\omega_0$	$\tilde{\zeta}_s^{\mathrm{B}}$	$\omega_s^{\mathrm{B}}/\omega_0$	$\tilde{V}_{\mathrm{LL}}^{(s)}$	$\tilde{V}_{\mathrm{SL}}^{(s)}$	$\tilde{g}_{s^3}$
1	3513	2.41×10^{-2}	2.24×10^{-2}	5.96×10^{-5}	1.57×10^{3}	9.06×10^{-3}	3.31×10^{-1}	1.00	1.76×10^{-2}
1′	3413	2.42×10^{-2}	3.39×10^{-2}	8.61×10^{-5}	1.29×10^{3}	9.75×10^{-3}	3.26×10^{-1}	1.00	0.132
2	1636	2.02×10^{-3}	8.32×10^{3}	8.90×10^{-3}	1.10×10^{3}	5.19×10^{-2}	2.97×10^{-1}	1.00	1.731

01 December 2025 21:12:15

Published under an exclusive license by AIP Publishing

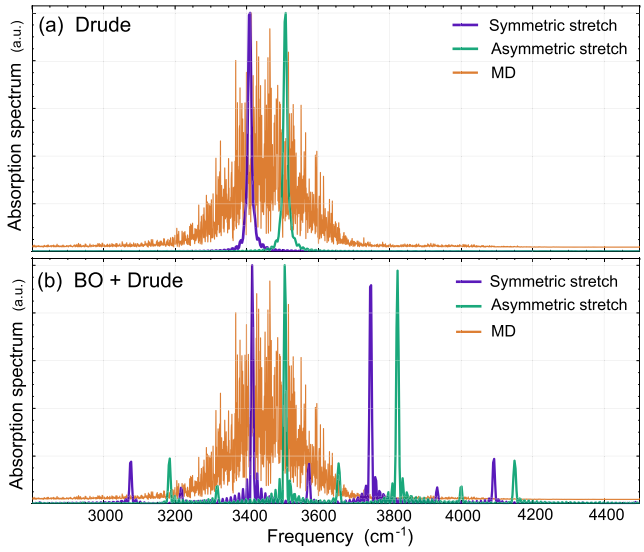

FIG. 3. Infrared absorption spectra of the (1) asymmetric stretch (green) and (1′) symmetric stretch (purple) modes under SL interaction, calculated via single-mode HEOM with optimized MAB parameters. (a) Drude SDF (Table I) and (b) BO+Drude SDF (Table V). MD results are shown in orange.

Fig. 3(b). Compared to the Drude-only case, the asymmetric stretching mode (green) exhibits two distinct split peaks centered around ~3650 cm^{-1}, along with several additional split peaks further out. Similarly, for the symmetric stretching mode (purple), split peaks are observed centered around ~3600 cm^{-1}. These split peaks are interpreted as phonon sidebands arising from strong coupling between the BO and the stretching modes.[55,56] The blue shift of the central peaks originates from the BO components of the counter term in Eq. (20). Such shifts are analogous to Stokes shifts in electronic spectroscopy, associated with the reorganization energy, $\lambda_s^{\mathrm{B}} = m_s \zeta_s^{\mathrm{B}}$.[55]

As previously discussed, the pronounced BO coupling likely originates from the bilinear interaction assumption inherent in the BO–SDF framework, despite the fact that inter- and intramolecular couplings are intrinsically anharmonic. Moreover, although low-frequency intermolecular motions are expected to behave classically, the BO scheme preserves coherence between inter- and intramolecular modes, thereby sharpening the splitting peaks. Consequently, this peak splitting is regarded as an artifact arising from the attempt to incorporate intermolecular vibrational effects within the BO–SDF framework. Thus, while the BO+Drude SDF yields better performance in trajectory optimization via MD compared to the Drude-only case, its ability to reproduce absorption spectra remains limited. To address this issue, the construction of an MAB model incorporating a fourth mode corresponding to intermolecular motion—thereby suppressing the BO coupling strength—should be examined.

We also calculated the infrared spectra for LL+SL interactions in (a) the Drude SDF and (b) the BO+Drude SDF using the parameter values listed in Table III and VII (results not shown).

The inclusion of the LL interaction resulted in no significant spectral change, except for a slight reduction in peak intensity at the high-frequency end. This finding supports the conclusion that the LL interaction plays a negligible role when the excitation frequency greatly exceeds thermal fluctuations[39] and justifies its omission for the stretching mode of water.

IV. CONCLUSION

We developed an ML algorithm that optimizes the parameters of the MAB model—a framework that captures intramolecular vibrational modes in concert with their surrounding environments—using MD trajectories as the foundational data source.

Cross-validation across diverse time windows and molecular systems confirms the model's generalizability beyond the training subsets. Key physical parameters remain stable under data resampling, underscoring the robustness of the proposed approach. The results enable precise determination of essential quantities, including anharmonic mode coupling and the characteristics of Drude and BO+Drude baths.

The developed algorithm faithfully captures both the precision of the input MD trajectories and the descriptive power of the optimized model, as reflected in the resulting IR spectrum. For instance, the S–B coupling of the bend mode and the BO-SDF of the stretch mode were overestimated due to limitations in the MD force field and the bilinear treatment of intermolecular and intramolecular modes in the BO-SDF framework, leading to artifacts in the sideband peaks. Therefore, reliable simulation of 2D IR spectra necessitates nuclear trajectories obtained from accurate MD force fields, ideally from quantum MD simulations.[17–20] In addition, the MAB model must be refined to incorporate not only nuclear trajectories but also spectroscopic features governed by optical dipole interactions and molecular polarizability. For example, our HEOM-based IR calculations demonstrate that LL interactions are not required for the stretch modes.

Although this work focuses on vibrational spectroscopy, the framework can be extended to model electronically excited states by replacing molecular dynamics with quantum mechanics/molecular mechanics (QM/MM) simulations.[36]

As part of ongoing methodological improvements, we plan to develop the HEOM code that can accommodate multiple vibrational modes, enabling the simulation of 2D IR spectra for water and other liquid systems.

ACKNOWLEDGMENTS

Y.T. was supported by JST (Grant No. CREST 1002405000170). K.P. acknowledges a fellowship supported by the JST SPRING program, The Establishment of University Fellowships Toward the Creation of Science and Technology Innovation (Grant No. JPMJSP2110). J.J. was supported by JSPS KAKENHI (Grant No. 24K23103).

01 December 2025 21:12:15

Published under an exclusive license by AIP Publishing

AUTHOR DECLARATIONS

Conflict of Interest

The authors have no conflicts to disclose.

Author Contributions

Kwanghee Park: Conceptualization (equal); Formal analysis (equal); Methodology (equal); Software (equal); Validation (equal); Writing – original draft (equal); Writing – review & editing (equal). **Ju-Yeon Jo**: Data curation (equal); Supervision (equal); Validation (equal); Writing – review & editing (equal). **Yoshitaka Tanimura**: Conceptualization (equal); Formal analysis (equal); Funding acquisition (equal); Writing – original draft (equal); Writing – review & editing (equal).

DATA AVAILABILITY

The data that support the findings of this study are available from the corresponding authors upon reasonable request.

APPENDIX A: FERGUSON POTENTIAL (FLEXIBLE SPC WATER)

Molecules are indexed by i,j; atomic sites within a molecule by $a,b \in \{\mathrm{O},\mathrm{H}_1,\mathrm{H}_2\}$. r_{OO}^{ij} is the O–O distance between molecules i and j. r_{ab} is the distance between site $a \in i$ and $b \in j$ (intermolecular). q_a are the partial charges and $k_e = 1/(4\pi\varepsilon_0)$. Lennard-Jones parameters are σ (size) and ε (well depth). Intramolecular geometry uses two O–H bond lengths, $r_{i,\mathrm{OH}_1}, r_{i,\mathrm{OH}_2}$, and the H–O–H angle θ_i. Stretch/bend parameters are (k_b, r_0) and (k_θ, θ_0), respectively. Unless noted, intramolecular nonbonded interactions are excluded by the topology.

The Ferguson model keeps SPC-style nonbonded interactions and introduces an anharmonic (cubic) O–H stretch plus a harmonic bend,

$$
\begin{aligned}
V_{\mathrm{Ferguson}} = \sum_{i<j}\left[4\varepsilon\left(\left(\frac{\sigma}{r_{OO}^{ij}}\right)^{12} - \left(\frac{\sigma}{r_{OO}^{ij}}\right)^{6}\right) + \sum_{a\in i}\sum_{b\in j}\frac{k_e\, q_a q_b}{r_{ab}}\right] \\
+ \sum_i \left[k_b\left(r_{i,\mathrm{OH}_1} - r_0\right)^2 + k_b k_{\mathrm{cub}}\left(r_{i,\mathrm{OH}_1} - r_0\right)^3\right. \\
+ k_b\left(r_{i,\mathrm{OH}_2} - r_0\right)^2 + k_b k_{\mathrm{cub}}\left(r_{i,\mathrm{OH}_2} - r_0\right)^3 \\
\left. + \frac{1}{2}k_\theta\left(\theta_i - \theta_0\right)^2\right]. \qquad \text{(A1)}
\end{aligned}
$$

Here, the cubic coefficient k_{cub} introduces asymmetry in the stretch potential about r_0, thereby improving vibrational behavior relative to a purely harmonic model; the bending motion remains harmonic about θ_0.

APPENDIX B: COORDINATE MAPPING

To evaluate training efficiency, we compared two distinct representations: one based on (a) Cartesian atomic coordinates and the other on (b) normal-mode vibrational coordinates. In the (a) Cartesian representation, the potential profile of the learnable system is optimized using internal coordinates, in particular, the two OH bond lengths, the HOH bending angle, and the SDF. Following optimization, the MAB model parameters are evaluated in the normal-mode coordinate space, denoted as q_s.

In contrast, under the framework referred to as case (b), each vibrational mode and its associated Liouvillian are constructed directly from Cartesian atomic coordinates. The effective potential $U_s(q_s)$ and $J_s(\omega)$ for each mode are subsequently optimized as functions of q_s. This approach enables more direct optimization with respect to the MAB variable q_s, rather than relying on atomic coordinates as in case (a).

Figure 4 presents a comparison of training and test losses for cases [(a) and (b)]. The normal mode framework exhibits faster convergence than the atomic framework, although its generality across molecular systems is reduced by the molecule-specific nature of normal modes. A further advantage of the normal mode formulation is that the objective function naturally decomposes by mode, facilitating mode-resolved diagnostics. Figure 5 illustrates the training losses

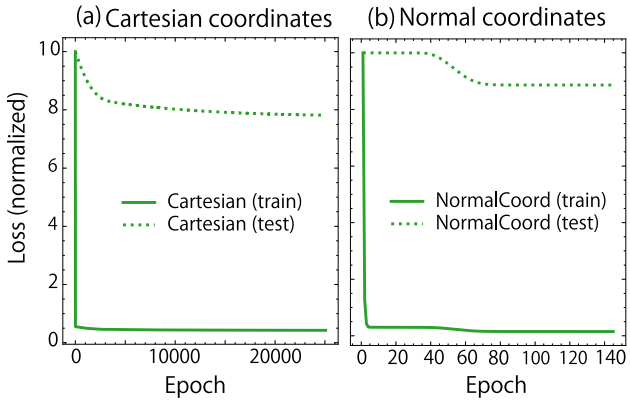

FIG. 4. Training and testing losses were evaluated by comparing predicted model trajectories with actual MD trajectories, using two coordinate systems: (a) atomic coordinates in Cartesian space and (b) normal-mode coordinates. In both cases, the system's time evolution was governed by the corresponding MD Liouvillian.

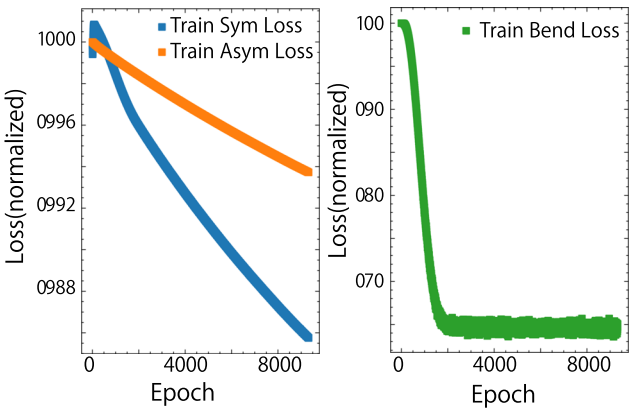

FIG. 5. Left panel shows the training losses for the OH symmetric and OH asymmetric stretch modes, while right panel displays the loss for the HOH bending mode. The bending mode demonstrates a more rapid learning process compared to the stretch modes.

01 December 2025 21:12:15

Published under an exclusive license by AIP Publishing

for the OH symmetric stretch, OH asymmetric stretch, and HOH bending modes. Notably, the bending mode converges substantially faster than the stretching modes.

APPENDIX C: EARLY STOPPING IN MODEL TRAINING

To mitigate overfitting and enhance generalization, early stopping[86] was applied to each model. Validation loss was monitored continuously, and training was halted upon stagnation or degradation of validation loss. In particular, a patience threshold of 300 epochs was employed. If the best validation loss remained unchanged for 300 consecutive epochs, early stopping was triggered. Upon activation, training resumed once with a reduced learning rate for a further 300 epochs. If no improvement occurred during this second phase, training was subsequently terminated. This protocol effectively mitigated overfitting while conservatively enabling escape from shallow plateaus via adaptive learning rate adjustment.

APPENDIX D: CROSS-VALIDATION

Model performance was assessed via cross-validation (CV). For each fold, the fitted physical parameters were recorded, and their inter-fold variation across folds was analyzed. This dispersion serves as a quantitative indicator of parameter stability and reflects the model's sensitivity to the choice of time windows and molecular subsets employed during training. The present analysis focuses on two key aspects: the representation of water molecules extracted from MD trajectories and the influence of the selected time window.

Accordingly, two distinct CV strategies were evaluated: molecule-level cross-validation (MOLVC) and time step cross-validation (TSCV). The MOLVC approach represents a scenario in which each molecule interacts with multiple baths, while the TSCV reflects a situation in which a single molecule interacts with a single bath over an extended duration. Notably, the molecule-level strategy systematically underestimates the strength of system–bath coupling. Therefore, the time step approach was adopted for subsequent evaluation.

1. Molecule-level cross-validation (MOLVC)

For molecule-level assessment, fourfold cross-validation was conducted over individual molecules. In each fold, three subsets were used for training and one for testing, with roles rotated such that each subset served as the test set once. This protocol ensured rigorous separation between training and testing data, enabling evaluation of the model's ability to generalize across distinct molecular configurations exhibiting potentially diverse dynamical behavior.

2. Time step cross-validation (TSCV)

Within the time step framework, data partitions were constructed to retain the temporal ordering of the dynamics. This approach is specifically intended to evaluate temporal consistency, requiring the model to produce forward predictions from earlier to later configurations. By preserving chronological order, this strategy enables a more realistic assessment of the model's predictive performance over time.

REFERENCES

[1] S. Mukamel, *Principles of Nonlinear Optical Spectroscopy* (Oxford University Press on Demand, 1999), Vol. 6.
[2] M. Cho, *Two-Dimensional Optical Spectroscopy* (CRC Press, 2009).
[3] P. Hamm and M. T. Zanni, *Concepts and Methods of 2D Infrared Spectroscopy* (Cambridge University Press, 2011).
[4] P. Hamm and A. Shalit, "Perspective: Echoes in 2D-Raman-THz spectroscopy," J. Chem. Phys. **146**, 130901 (2017).
[5] T. l. C. Jansen, S. Saito, J. Jeon, and M. Cho, "Theory of coherent two-dimensional vibrational spectroscopy," J. Chem. Phys. **150**, 100901 (2019).
[6] S. Saito and I. Ohmine, "Fifth-order two-dimensional Raman spectroscopy of liquid water, crystalline ice ih and amorphous ices: Sensitivity to anharmonic dynamics and local hydrogen bond network structure," J. Chem. Phys. **125**, 084506 (2006).
[7] T. Hasegawa and Y. Tanimura, "Calculating fifth-order Raman signals for various molecular liquids by equilibrium and nonequilibrium hybrid molecular dynamics simulation algorithms," J. Chem. Phys. **125**, 074512 (2006).
[8] Y. L. Li, L. Huang, R. J. Dwayne Miller, T. Hasegawa, and Y. Tanimura, "Two-dimensional fifth-order Raman spectroscopy of liquid formamide: Experiment and theory," J. Chem. Phys. **128**, 234507 (2008).
[9] T. Hasegawa and Y. Tanimura, "Nonequilibrium molecular dynamics simulations with a backward–forward trajectories sampling for multidimensional infrared spectroscopy of molecular vibrational modes," J. Chem. Phys. **128**, 064511 (2008).
[10] Z. Pan, T. Wu, T. Jin, Y. Liu, Y. Nagata, R. Zhang, and W. Zhuang, "Low frequency 2D Raman-THz spectroscopy of ionic solution: A simulation study," J. Chem. Phys. **142**, 212419 (2015).
[11] H. Ito, T. Hasegawa, and Y. Tanimura, "Calculating two-dimensional THz-Raman-THz and Raman-THz-THz signals for various molecular liquids: The samplers," J. Chem. Phys. **141**, 124503 (2014).
[12] H. Ito, T. Hasegawa, and Y. Tanimura, "Effects of intermolecular charge transfer in liquid water on Raman spectra," J. Phys. Chem. Lett. **7**, 4147–4151 (2016).
[13] T. Steinel, J. B. Asbury, S. A. Corcelli, C. P. Lawrence, J. L. Skinner, and M. D. Fayer, "Water dynamics: Dependence on local structure probed with vibrational echo correlation spectroscopy," Chem. Phys. Lett. **386**, 295–300 (2004).
[14] A. Ishizaki and Y. Tanimura, "Nonperturbative Non-Markovian quantum master equation: Validity and limitation to calculate nonlinear response functions," Chem. Phys. **347**, 185–193 (2008), a part of Special Issue: Ultrafast Photoinduced Processes in Polyatomic Molecules.
[15] Y. Tanimura and A. Ishizaki, "Modeling, calculating, and analyzing multidimensional vibrational spectroscopies," Acc. Chem. Res. **42**, 1270–1279 (2009).
[16] Y. Tanimura, "Numerically 'exact' approach to open quantum dynamics: The hierarchical equations of motion (HEOM)," J. Chem. Phys. **153**, 020901 (2020).
[17] X. Liu and J. Liu, "Critical role of quantum dynamical effects in the Raman spectroscopy of liquid water," Mol. Phys. **116**, 755–779 (2018).
[18] J. Liu, W. H. Miller, G. S. Fanourgakis, S. S. Xantheas, S. Imoto, and S. Saito, "Insights in quantum dynamical effects in the infrared spectroscopy of liquid water from a semiclassical study with an *ab initio*-based flexible and polarizable force field," J. Chem. Phys. **135**, 244503 (2011).
[19] G. R. Medders and F. Paesani, "Infrared and Raman spectroscopy of liquid water through 'first-principles' many-body molecular dynamics," J. Chem. Theory Comput. **11**, 1145–1154 (2015).
[20] K. M. Hunter, F. A. Shakib, and F. Paesani, "Disentangling coupling effects in the infrared spectra of liquid water," J. Phys. Chem. B **122**, 10754–10761 (2018).
[21] M. Cho, G. R. Fleming, S. Saito, I. Ohmine, and R. M. Stratt, "Instantaneous normal mode analysis of liquid water," J. Chem. Phys. **100**, 6672–6683 (1994).
[22] A. Paarmann, T. Hayashi, S. Mukamel, and R. J. D. Miller, "Nonlinear response of vibrational excitons: Simulating the two-dimensional infrared spectrum of liquid water," J. Chem. Phys. **130**, 204110 (2009).
[23] J. R. Schmidt, S. A. Corcelli, and J. L. Skinner, "Pronounced non-Condon effects in the ultrafast infrared spectroscopy of water," J. Chem. Phys. **123**, 044513 (2005).
[24] T. l. C. Jansen, B. M. Auer, M. Yang, and J. L. Skinner, "Two-dimensional infrared spectroscopy and ultrafast anisotropy decay of water," J. Chem. Phys. **132**, 224503 (2010).

01 December 2025 21:12:15

Published under an exclusive license by AIP Publishing

[25]A. Sakurai and Y. Tanimura, "Does $\hbar$ play a role in multidimensional spectroscopy? Reduced hierarchy equations of motion approach to molecular vibrations," J. Phys. Chem. A **115**, 4009–4022 (2011).
[26]T. Ikeda, H. Ito, and Y. Tanimura, "Analysis of 2D THz-Raman spectroscopy using a Non-Markovian Brownian oscillator model with nonlinear system-bath interactions," J. Chem. Phys. **142**, 212421 (2015).
[27]H. Ito and Y. Tanimura, "Simulating two-dimensional infrared-Raman and Raman spectroscopies for intermolecular and intramolecular modes of liquid water," J. Chem. Phys. **144**, 074201 (2016).
[28]H. Takahashi and Y. Tanimura, "Discretized hierarchical equations of motion in mixed Liouville–Wigner space for two-dimensional vibrational spectroscopies of liquid water," J. Chem. Phys. **158**, 044115 (2023); arXiv:2302.09799.
[29]H. Takahashi and Y. Tanimura, "Simulating two-dimensional correlation spectroscopies with third-order infrared and fifth-order infrared–Raman processes of liquid water," J. Chem. Phys. **158**, 124108 (2023); arXiv:2302.09760.
[30]R. Hoshino and Y. Tanimura, "Analysis of intramolecular modes of liquid water in two-dimensional spectroscopy: A classical hierarchical equations of motion approach," J. Chem. Phys. **162**, 044105 (2025).
[31]R. Hoshino and Y. Tanimura, "A multimode classical hierarchical Fokker–Planck equations approach to molecular vibrations: Simulating two-dimensional spectra," J. Chem. Phys. **163**, 172501 (2025).
[32]Y. Tanimura, "Stochastic Liouville, Langevin, Fokker–Planck, and master equation approaches to quantum dissipative systems," J. Phys. Soc. Jpn. **75**, 082001 (2006).
[33]T. Steffen and Y. Tanimura, "Two-dimensional spectroscopy for harmonic vibrational modes with nonlinear system-bath interactions. I. Gaussian–White case," J. Phys. Soc. Jpn. **69**, 3115–3132 (2000).
[34]Y. Tanimura and T. Steffen, "Two-Dimensional spectroscopy for harmonic vibrational modes with nonlinear system-bath interactions. II. Gaussian–Markovian case," J. Phys. Soc. Jpn. **69**, 4095–4106 (2000).
[35]S. Ueno and Y. Tanimura, "Modeling intermolecular and intramolecular modes of liquid water using multiple heat baths: Machine learning approach," J. Chem. Theory Comput. **16**, 2099–2108 (2020).
[36]S. Ueno and Y. Tanimura, "Modeling and simulating the excited-state dynamics of a system with condensed phases: A machine learning approach," J. Chem. Theory Comput. **17**, 3618–3628 (2021).
[37]T. Kato and Y. Tanimura, "Vibrational spectroscopy of a harmonic oscillator system nonlinearly coupled to a heat bath," J. Chem. Phys. **117**, 6221–6234 (2002).
[38]T. Kato and Y. Tanimura, "Two-dimensional Raman and infrared vibrational spectroscopy for a harmonic oscillator system nonlinearly coupled with a colored noise bath," J. Chem. Phys. **120**, 260–271 (2004).
[39]A. Ishizaki and Y. Tanimura, "Modeling vibrational dephasing and energy relaxation of intramolecular anharmonic modes for multidimensional infrared spectroscopies," J. Chem. Phys. **125**, 084501 (2006).
[40]K. Okumura and Y. Tanimura, "Two-time correlation functions of a harmonic system nonbilinearly coupled to a heat bath: Spontaneous Raman spectroscopy," Phys. Rev. E **56**, 2747–2750 (1997).
[41]Y. Tanimura and P. G. Wolynes, "Quantum and classical Fokker–Planck equations for a Gaussian–Markovian noise bath," Phys. Rev. A **43**, 4131–4142 (1991).
[42]C. P. Lawrence and J. L. Skinner, "Vibrational spectroscopy of HOD in liquid D_2O. I. Vibrational energy relaxation," J. Chem. Phys. **117**, 5827–5838 (2002).
[43]C. P. Lawrence and J. L. Skinner, "Vibrational spectroscopy of HOD in liquid D_2O. II. Infrared line shapes and vibrational stokes shift," J. Chem. Phys. **117**, 8847–8854 (2002).
[44]C. P. Lawrence and J. L. Skinner, "Vibrational spectroscopy of HOD in liquid D_2O. III. Spectral diffusion, and hydrogen-bonding and rotational dynamics," J. Chem. Phys. **118**, 264–272 (2003).
[45]A. Piryatinski, C. P. Lawrence, and J. L. Skinner, "Vibrational spectroscopy of hod in liquid D_2O. IV. Infrared two-pulse photon echoes," J. Chem. Phys. **118**, 9664–9671 (2003).
[46]A. Piryatinski, C. P. Lawrence, and J. L. Skinner, "Vibrational spectroscopy of HOD in liquid D_2O. V. Infrared three-pulse photon echoes," J. Chem. Phys. **118**, 9672–9679 (2003).
[47]C. P. Lawrence and J. L. Skinner, "Vibrational spectroscopy of HOD in liquid D_2O. VI. Intramolecular and intermolecular vibrational energy flow," J. Chem. Phys. **119**, 1623–1633 (2003).
[48]C. P. Lawrence and J. L. Skinner, "Vibrational spectroscopy of HOD in liquid D_2O. VII. Temperature and frequency dependence of the OH stretch lifetime," J. Chem. Phys. **119**, 3840–3848 (2003).
[49]T. Yagasaki and S. Saito, "Ultrafast intermolecular dynamics of liquid water: A theoretical study on two-dimensional infrared spectroscopy," J. Chem. Phys. **128**, 154521 (2008).
[50]T. Yagasaki and S. Saito, "A novel method for analyzing energy relaxation in condensed phases using nonequilibrium molecular dynamics simulations: Application to the energy relaxation of intermolecular motions in liquid water," J. Chem. Phys. **134**, 184503 (2011).
[51]T. Yagasaki and S. Saito, "Fluctuations and relaxation dynamics of liquid water revealed by linear and nonlinear spectroscopy," Annu. Rev. Phys. Chem. **64**, 55–75 (2013).
[52]S. Imoto, S. S. Xantheas, and S. Saito, "Ultrafast dynamics of liquid water: Frequency fluctuations of the OH stretch and the HOH bend," J. Chem. Phys. **139**, 044503 (2013).
[53]S. Imoto, S. S. Xantheas, and S. Saito, "Ultrafast dynamics of liquid water: Energy relaxation and transfer processes of the OH stretch and the HOH bend," J. Phys. Chem. B **119**, 11068–11078 (2015).
[54]Y. Tanimura and R. Kubo, "Time evolution of a quantum system in contact with a nearly Gaussian–Markoffian noise bath," J. Phys. Soc. Jpn. **58**, 101–114 (1989).
[55]Y. Tanimura and S. Mukamel, "Optical Stark spectroscopy of a Brownian oscillator in intense fields," J. Phys. Soc. Jpn. **63**, 66–77 (1994).
[56]Y. Tanimura, "Reduced hierarchy equations of motion approach with Drude plus Brownian spectral distribution: Probing electron transfer processes by means of two-dimensional correlation spectroscopy," J. Chem. Phys. **137**, 22A550 (2012).
[57]M. Tanaka and Y. Tanimura, "Quantum dissipative dynamics of electron transfer reaction system: Nonperturbative hierarchy equations approach," J. Phys. Soc. Jpn. **78**, 073802 (2009).
[58]M. Tanaka and Y. Tanimura, "Multistate electron transfer dynamics in the condensed phase: Exact calculations from the reduced hierarchy equations of motion approach," J. Chem. Phys. **132**, 214502 (2010).
[59]A. G. Dijkstra and Y. Tanimura, "Linear and third- and fifth-order nonlinear spectroscopies of a charge transfer system coupled to an underdamped vibration," J. Chem. Phys. **142**, 212423 (2015).
[60]S. Chandrasekaran, M. Aghtar, S. Valleau, A. Aspuru-Guzik, and U. Kleinekathöfer, "Influence of force fields and quantum chemistry approach on spectral densities of BChl *a* in solution and in FMO proteins," J. Phys. Chem. B **119**, 9995–10004 (2015).
[61]Y. Fujihashi, G. R. Fleming, and A. Ishizaki, "Impact of environmentally induced fluctuations on quantum mechanically mixed electronic and vibrational pigment states in photosynthetic energy transfer and 2D electronic spectra," J. Chem. Phys. **142**, 212403 (2015).
[62]M. Cainelli, R. Borrelli, and Y. Tanimura, "Effect of mixed Frenkel and charge transfer states in time-gated fluorescence spectra of perylene bisimides H-aggregates: Hierarchical equations of motion approach," J. Chem. Phys. **157**, 084103 (2022).
[63]I. Ohmine and H. Tanaka, "Fluctuation, relaxations, and hydration in liquid water. Hydrogen-bond rearrangement dynamics," Chem. Rev. **93**, 2545–2566 (1993).
[64]I. Ohmine and S. Saito, "Water dynamics: Fluctuation, relaxation, and chemical reactions in hydrogen bond network rearrrngement," Acc. Chem. Res. **32**, 741–749 (1999).
[65]E. T. J. Nibbering and T. Elsaesser, "Ultrafast vibrational dynamics of hydrogen bonds in the condensed phase," Chem. Rev. **104**(4), 1887–1914 (2004).
[66]B. Bagchi, *Water in Biological and Chemical Processes: From Structure and Dynamics to Function* (Cambridge University Press, 2013).
[67]D. Kraemer, M. L. Cowan, A. Paarmann, N. Huse, E. T. J. Nibbering, T. Elsaesser, and R. J. D. Miller, "Temperature dependence of the two-dimensional

01 December 2025 21:12:15

Published under an exclusive license by AIP Publishing

infrared spectrum of liquid H_2O," Proc. Natl. Acad. Sci. U. S. A. **105**, 437–442 (2008).
[68]L. De Marco, J. A. Fournier, M. Thämer, W. Carpenter, and A. Tokmakoff, "Anharmonic exciton dynamics and energy dissipation in liquid water from two-dimensional infrared spectroscopy," J. Chem. Phys. **145**, 094501 (2016).
[69]W. B. Carpenter, J. A. Fournier, R. Biswas, G. A. Voth, and A. Tokmakoff, "Delocalization and stretch-bend mixing of the HOH bend in liquid water," J. Chem. Phys. **147**, 084503 (2017).
[70]N. H. C. Lewis, B. Dereka, Y. Zhang, E. J. Maginn, and A. Tokmakoff, "From networked to isolated: Observing water hydrogen bonds in concentrated electrolytes with two-dimensional infrared spectroscopy," J. Phys. Chem. B **126**, 5305–5319 (2022).
[71]L. Chuntonov, R. Kumar, and D. G. Kuroda, "Non-linear infrared spectroscopy of the water bending mode: Direct experimental evidence of hydration shell reorganization?," Phys. Chem. Chem. Phys. **16**, 13172–13181 (2014).
[72]M. Grechko, T. Hasegawa, F. D'Angelo, H. Ito, D. Turchinovich, Y. Nagata, and M. Bonn, "Coupling between intra- and intermolecular motions in liquid water revealed by two-dimensional terahertz-infrared-visible spectroscopy," Nat. Commun. **9**, 885 (2018).
[73]L. Vietze, E. H. G. Backus, M. Bonn, and M. Grechko, "Distinguishing different excitation pathways in two-dimensional terahertz-infrared-visible spectroscopy," J. Chem. Phys. **154**, 174201 (2021).
[74]T. Begušić and G. A. Blake, "Two-dimensional infrared-Raman spectroscopy as a probe of water's tetrahedrality," Nat. Commun. **14**, 1950 (2023).
[75]P. Hamm and J. Savolainen, "Two-dimensional-Raman-terahertz spectroscopy of water: Theory," J. Chem. Phys. **136**, 094516 (2012).
[76]P. Hamm, J. Savolainen, J. Ono, and Y. Tanimura, "Note: Inverted time-ordering in two-dimensional-Raman-terahertz spectroscopy of water," J. Chem. Phys. **136**, 236101 (2012).
[77]J. Savolainen, S. Ahmed, and P. Hamm, "Two-dimensional Raman–terahertz spectroscopy of water," Proc. Natl. Acad. Sci. U. S. A. **110**, 20402–20407 (2013).
[78]P. Hamm, "2D-Raman-THz spectroscopy: A sensitive test of polarizable water models," J. Chem. Phys. **141**, 184201 (2014).
[79]J. Hu, R.-X. Xu, and Y. Yan, "Communication: Padé spectrum decomposition of Fermi function and Bose function," J. Chem. Phys. **133**, 101106 (2010).
[80]M. J. Abraham, T. Murtola, R. Schulz, S. Páll, J. C. Smith, B. Hess, and E. Lindahl, "GROMACS: High performance molecular simulations through multi-level parallelism from laptops to supercomputers," SoftwareX **1-2**, 19–25 (2015).
[81]D. M. Ferguson, "Parameterization and evaluation of a flexible water model," J. Comput. Chem. **16**, 501–511 (1995).
[82]T. Hasegawa and Y. Tanimura, "A polarizable water model for intramolecular and intermolecular vibrational spectroscopies," J. Phys. Chem. B **115**, 5545–5553 (2011).
[83]V. Babin, C. Leforestier, and F. Paesani, "Development of a "First Principles" water potential with flexible monomers: Dimer potential energy surface, VRT spectrum, and second virial coefficient," J. Chem. Theory Comput. **9**, 5395–5403 (2013).
[84]V. Babin, G. R. Medders, and F. Paesani, "Development of a 'First Principles' water potential with flexible monomers. II: Trimer potential energy surface, third virial coefficient, and small clusters," J. Chem. Theory Comput. **10**, 1599–1607 (2014).
[85]G. R. Medders, V. Babin, and F. Paesani, "Development of a 'first-principles' water potential with flexible monomers. III. Liquid phase properties," J. Chem. Theory Comput. **10**, 2906–2910 (2014).
[86]C. Wang, S. Venkatesh, and J. Judd, "Optimal stopping and effective machine complexity in learning," in *Advances in Neural Information Processing Systems*, edited by J. Cowan, G. Tesauro, and J. Alspector (Morgan-Kaufmann, 1993), Vol. 6.

01 December 2025 21:12:15

Published under an exclusive license by AIP Publishing